RESEARCH ARTICLE | JUNE 02 2025

Controlling deposition and characterizing dynamics of thin liquid films with high temporal and spatial resolution

G. Le Lay ; A. Daerr

Physics of Fluids 37, 062101 (2025)
https://doi.org/10.1063/5.0268672

Physics of Fluids ARTICLE pubs.aip.org/aip/pof

Controlling deposition and characterizing dynamics of thin liquid films with high temporal and spatial resolution

Cite as: Phys. Fluids **37**, 062101 (2025); doi: 10.1063/5.0268672
Submitted: 3 March 2025 · Accepted: 16 April 2025 ·
Published Online: 2 June 2025

View Online Export Citation CrossMark

G. Le Lay[a] and A. Daerr

AFFILIATIONS

Matière et Systèmes Complexes UMR 7057 Université Paris Cité, CNRS, 75231 Paris cedex 13, France

[a]Author to whom correspondence should be addressed: gregoire.le-lay@u-paris.fr

ABSTRACT

The high inertia of classical fluid coating processes severely limits the possibility of controlling the deposited film thickness through the entrainment velocity. We describe and characterize a new experimental device where the inertia is dramatically reduced, allowing for millimeter-scale patterning with micrometer-accurate thickness. Measuring precise film profiles over large spatial extents with high temporal resolution poses a challenge, which we overcome using a custom interferometric setup coupled with state-of-the-art signal processing. The sensitivity of our method allows us to resolve film thinning rates in the nanometer-per-second range and to quantify the relative contribution of surface-tension and gravity-driven flows. We apply this method by showing that the thickness of the deposited film obeys the classical Landau–Levich scaling even when the meniscus faces important acceleration.

I. INTRODUCTION

Fluid entrainment by a moving substrate is of interest in many contexts, notably as a process to coat solids with thin layers. From wire insulation to the modification of optical and surface properties of window glass, controlling the thickness and uniformity of fluid layers is of key importance. The possibility to create textures is also increasingly explored, e.g., by controlling instabilities arising in the presence of evaporation.[1,2] In confined flows, the entrainment transition governs the pressure head required to drive multi-phase flows such as Taylor bubbles, because of the high viscous dissipation in the displaced menisci. This is of importance because these flows arise in many different applications, including the study and design of microfluidic devices,[3] or the prevention of airway obstruction in a biomedical context.[4,5] Lastly, multi-phase flows are of particular interest in the study of vapor–liquid mass exchange in heat pipes.[6] In this domain, thin films have gained attention as an efficient way to improve transport in capillary-driven heat exchangers[7,8] and require understanding its evolution in non-stationary systems such as loop heat pipes.[9]

The thickness of an entrained film has been studied in various geometries, such as flat plates,[10–13] capillaries,[14,15] or fibers.[16] Its asymptotic scaling was derived by Landau–Levich–Derjaguin (LLD),[17–19] who showed that the steady-state film thickness of the fluid layer of viscosity η and surface tension γ entrained by a planar solid pulled from a bath results from the compensation of viscous stresses by capillary pressure gradients at the bulk-film transition. Limits and corrections to this famous result have been extensively explored,[16,20] such as effects of gravity, evaporation, Marangoni forces in the presence of surfactants,[21] wetting dynamics near contact lines,[22,23] non-Newtonian rheology/suspensions, or inertial and boundary layer effects at high speeds.[24]

In order to visualize and quantitatively measure the features of the entrained films, several techniques are used in the literature. Direct optical visualization of the system only allows one to see the meniscus, which refracts light strongly, but prevents measurements on the film itself.[25] The thickness of a very thin film can be precisely measured at one point, either by spectrometry of the reflected signal[26,27] or by measuring the displacement of the focus points of a laser.[28] Profiles can be captured by displacing the point probe, if the film evolution is periodic or stationary. Alternatively, the film profile can be reconstructed by analyzing the optical distortion of a grid as seen through the interface,[27] with a spatial resolution limited by the grid spacing. The visualization of one-directional interference patterns for different wavelengths[29] also allows to measure the film profile. Often, several of these techniques are used in combination in order to cumulate their advantages.

The purpose of this paper is to present an original setup to deposit and characterize films of controllable thickness through the displacement of a fluid rivulet in a Hele–Shaw geometry.

We explore the potential of this system for non-uniform, high-dynamic range coating and show that the film can be modulated at sub-micrometer scale in thickness and at sub-millimeter scale in the direction of meniscus motion. This is possible because the moving fluid phase has a very small volume so that its inertia is vastly reduced almost to that of the surrounding gas phase, in stark contrast to the bulk displacement of one fluid by another as studied by Saffman and Taylor[30] and Tabeling *et al.*,[31] or to moving substrate configurations. Fast acceleration can, therefore, be achieved by moderate pressure jumps.

We monitor the film evolution using an interferometric measurement technique to study the structure and dynamics of the deposited film with both high spatial and temporal resolution. The precision of the obtained profiles is such that we can quantify the contribution of surface-tension induced flows that depend on the fourth-order spatial derivative and compare it to the gravitational drainage. We are also able to verify that the Landau–Levich–Dejarguin (LLD) scaling for the film thickness holds even when the meniscus accelerates from static to maximum velocity on a length scale roughly equal to the outer meniscus scale.

After describing our experimental setup in Sec. II and measurement method in Sec. III, the investigation of the influence of capillary flow vs gravitational drainage is investigated in Sec. IV, and the relation of film height to meniscus speed for a sinusoidally driven liquid bridge is studied in Sec. V.

II. FILM DEPOSITION AND OBSERVATION

To generate a very thin layer of liquid of controlled height on a substrate, we use the displacement of a liquid stream in an air-filled Hele–Shaw cell. Between two glass plates (commercial float window glass, dimensions 1 m × 10 cm × 6 mm) separated by a small gap b, we inject a continuous stream of liquid so that it wets both plates, forming a liquid bridge between them in which the fluid flows downwards under the action of gravity. The liquid stream consisting in this vertically extended bridge laterally delimited by two semicircular menisci is henceforth termed rivulet. The vertical, or streamwise, direction defines the *x-axis* oriented with gravity. The z direction in which the rivulet can move is termed transverse, and y corresponds to the gapwise direction, being perpendicular to the plates.

The liquid we use in this article is a perfluorinated oil (density $\rho = 1.72\,\mathrm{g/cm^3}$, kinematic viscosity $\nu = 1.00\,\mathrm{cSt}$, surface tension $\gamma = 14\,\mathrm{mN/m}$, refractive index $n = 1.26$), and we set the gap between the plates to $b = 0.6\,\mathrm{mm}$. We assume total wetting between the oil and the glass plates: a drop spreading experiment confirms that the oil wets the glass with a contact angle smaller than 0.5°. We inject the liquid using a gear pump through silicone tubing. The rivulet falls down vertically, and this situation is stable while we stay under a critical flow rate.[32] However, the rivulet can be locally displaced by imposing a pressure difference between the right and left sides of the cell. Indeed, since the rivulet separates the cell vertically in two parts and since it is airtight, it behaves like a "liquid membrane" and can be pushed transversally using an imposed pressure difference between both sides—or, equivalently, by pushing it with an asymmetric air flow. In our experiments, we use loudspeakers on both sides of the cell to control the lateral movement of the rivulet. By feeding these speakers opposite signals, when the membrane of one advances, the membrane of the other retracts, pushing the rivulet in the same direction.[33] Note that by introducing immobile obstructing elements inside the cell, we can change the geometry of the air flow generated by the speakers and locally modulate the amplitude of movement of the rivulet.

While moving, the menisci deposit behind them very thin liquid films (see Fig. 1), which are the main object of study of this paper. By imposing the signal sent to the speakers, the movement of the rivulet can be precisely controlled. This allows for deterministic and reproducible film deposition on the plates.

To measure with precision the geometry of such a very thin film (no thicker than 10 μm) as well as its temporal evolution is an experimental challenge. To adopt an unambiguous convention, we henceforth call height and note $h(x, z, t)$ the spatial extent in the y direction (which also corresponds to the depth, or thickness) of the film. The films have extremely high aspect ratio, with their height being around a thousand time smaller than their transverse and streamwise extent. To maximize the resolution in all directions while maintaining a high temporal resolution, we use an interferometric method. As will be shown later, this allows us to measure microscopic changes of film depth over a macroscopic space scale on the other directions, while temporally resolving all phenomena of interest. We use monochromatic lighting (high-pressure sodium–vapor lamp, $\lambda_0 = 589\,\mathrm{nm}$) to visualize the film. The light reflected by the glass–oil and oil–air interfaces creates an interference pattern that we observe using a beam splitter and a camera as shown in Fig. 1. Through this manuscript, we use the term *luminosity* to denote the quantity of light captured during exposure by a single camera pixel. Since our camera uses 8-bit pixel depth, this quantity, which is proportional to the local light intensity, is comprised between 0 and 255. We use an AVT Manta G-223B camera controlled by the open-source software Limrendir to record the experimental sequence of images. We mount a telecentric lens (Myutron MGTL10V) on this camera in order to select the light that arrives normal to the glass surface. Note that since the menisci limiting the rivulet touch the front and back plates, they leave films on both. The shallow depth of field (0.43 mm, manufacturer data) of our lens allows us to selectively focus on the film deposited on the frontmost plate. Light backscattered from the back plate and from the outer glass–air interfaces of the Hele–Shaw cell is out-of-focus and therefore contributes only to a uniform base signal.

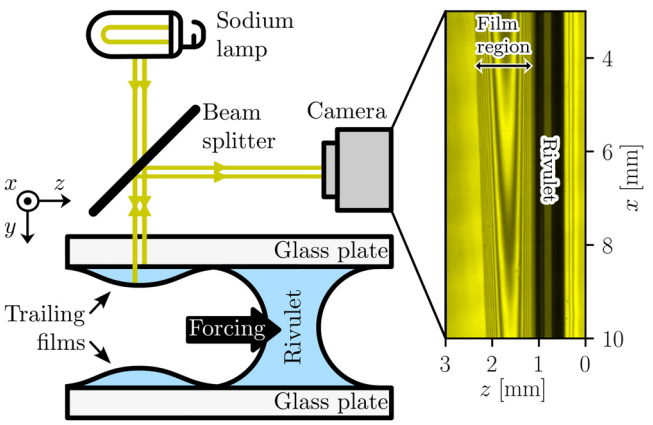

FIG. 1. Visualization setup (proportions not to scale). The rivulet moves under the effect of the forcing, leaving a trailing film of liquid behind it. The interference pattern due to the light being refracted on both interfaces of the front film is observed by a camera.

The images we obtain consist in successions of bright and dark interference fringes, which correspond to "iso-height" level lines of the film. Since the topology of the film is encoded in the fringes, it is possible to demodulate the luminosity signal in order to find the height profile of the film. In this article, the main procedure we use to deduce the height profile of the file use the following four steps: (1) the signal is cleaned, removing insignificant noise: high-frequency components corresponding to noise on the camera sensor, and low-frequency components corresponding to the loss of contrast due to the fringes being very close from one another; (2) the instantaneous phase of the resulting signal is obtained, typically by using a Hilbert transform (i.e., by appropriately masking the Fourier transform of the signal) or by detecting the extrema points/lines corresponding to bright or dark fringes; (3) the resulting phase is unwrapped so that the 0-phase point corresponds to the absence (0-height) of film; and (4) the phase information is converted into height information using the interference condition. Indeed, the luminosity of a fringe depends on the value of the phase difference between the interfering light rays $\Phi = 2\pi \frac{2h}{\lambda}$, where $\lambda = \lambda_0/n$ is the wavelength of the light inside the liquid. Between two fringes of opposite brightness, the height difference corresponds to a phase difference of $\Phi = \pi$. This corresponds to $h_0 \triangleq \lambda/4 \approx 117$ nm. This means that we are able to measure variations of height corresponding to one-tenth of a micrometer on spatial scales going from 10 µm (distance between adjacent pixel midpoints, lens magnification is 1.0) to 10 mm (total field of view of the camera). Thus, we can monitor the evolution of the geometry of the whole film on arbitrary short (or long) timescales by modifying the frame rate of the camera. All the source code and analysis routines used to obtain the figures in this article, as well as the relevant raw data, are available in an open-access repository[34] containing all necessary details and instructions.

The typical geometry of a film we are interested in is shown in Fig. 2. The changes of luminosity on the image translate to changes of height of the film, which we are able to quantitatively deduce, as shown in the figure. Note that for the images presented in this article, the color scheme has been chosen in order to present a visible contrast between dark and bright interference fringes. Usually, our films have a transverse section ($h(z)$) looking like half of a very flat ellipse (with a high aspect ratio, of order 1000/1), and the height varies very slowly with the x coordinate (with very shallow slopes, of order 10^{-4}).

In this study, we will be interested in the films generated by two different kinds of rivulet movement.

In the first part, we look at films generated by a fast and sudden movement of the rivulet. This snapping motion leaves behind the rivulet an initially thick film, the evolution of which we can monitor over long timescales. This allows us to show that precise measurements are possible using our method, and we show that, thanks to our high space and time resolution, we are able to quantitatively explain the evolution of the film geometry as a function of time.

In a second part, we are interested in films left behind by rivulets adopting a periodic motion. This allows us to demonstrate that we can create highly reproducible films with a precisely controlled geometry.

III. SPACE-TIME EVOLUTION

By imposing a snapping motion to the rivulet, we create a film with a relatively sharp transverse profile, due to the rapid change of deposition speed during the movement. We then monitor the time evolution of the film, measuring the change in its geometric properties with time. When relaxing, the geometry of the film changes in two ways: its cross section flattens, and the height of its crest line decreases due to liquid drainage. In this paper, we call crest the curve along the x direction formed by all the maxima along the transverse direction, as illustrated in Fig. 2.

As is shown in Fig. 3, we are able to measure the height of the crest h_{crest} as a function of space at different times. As one can notice, the film drains as time goes on, and the height of its crest (and the rest

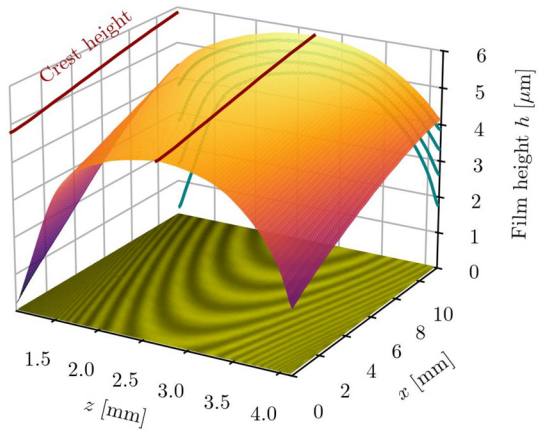

FIG. 2. Height profile of a liquid film as a function of the vertical (x) and transverse (z) coordinates. In this illustration image, the origins of the axes are arbitrary. The crest is indicated by a dark red line. Some transverse cross sections at various x coordinates are projected to the back, in blue.

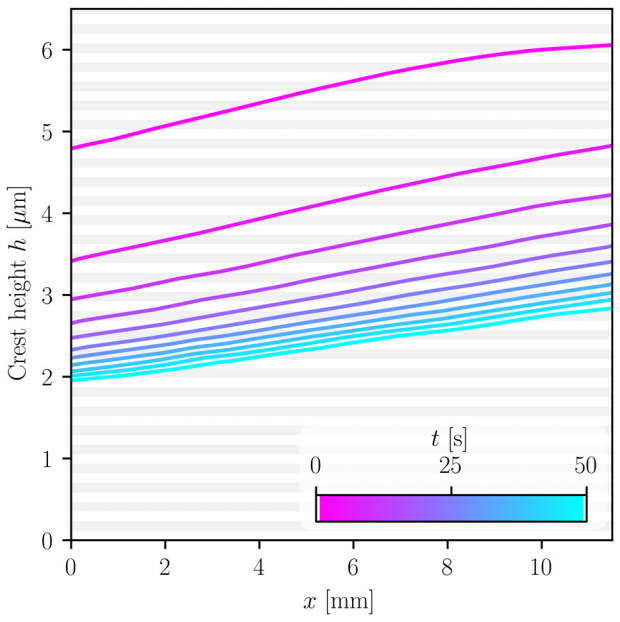

FIG. 3. Evolution of crest height h_{crest} as a function of space (bottom axis) for different times (color/grayscale). The alternating white and gray horizontal lines have a width (and spacing) of $h_0 = \lambda/4$. They allow to visualize the interference fringes crossed along a crest line.

of the film) diminishes with time. The film also has a slope, due to inhomogeneities of the rivulet movement amplitude.

Thanks to the high time resolution our method allows, we can do even better and push the measurement of the crest height to its limit by visualizing the entire field $h_{\text{crest}}(x,t)$. This is done by gathering the light signal along the crest line at every frame with a high frame rate (50 frame/s). The luminosity along the crest as a function of time and space is shown in Fig. 4 (left).

We can use this information to obtain the phase of the signal. A two-dimensional Hilbert transform is used to recover the phase of the corresponding analytic signal. Using the instantaneous phase $\Phi(x,t)$ of our signal, we can then reconstruct the entire crest height profile, thanks to the relation $h = \lambda\,\Phi/(4\pi)$. The results of this height-extraction process are shown in Fig. 4 (right). In this figure, we plotted on both spatiotemporal profiles the level lines corresponding to $h = N\,h_0$, with N an integer being even (black dashed lines) or odd (white dashed lines). As one can visually confirm, these levels correspond to the bright and dark interference fringes, since they correspond to constructive and destructive interference conditions, respectively, for the reflected light. We are then able to use this information to quantitatively understand the height evolution mechanism.

IV. FILM DRAINAGE

We have shown that we can experimentally access many metrics that are difficult to measure, such as the height profile h_{crest}, its slope $\partial_x h_{\text{crest}}$, and even its evolution with time $\partial_t h_{\text{crest}}$. We show in this section that we can quantitatively link these variables, confirming the relevance and the precision of our measurements.

The time evolution of the height $h(x,z,t)$ of the film is dictated by the thin film equation for a Newtonian fluid with no surface shear on a vertical substrate. It reads

$$\frac{\partial h}{\partial t} = -\nabla\cdot\mathbf{q} - \Phi_{\text{evap}} \quad \text{with} \quad \mathbf{q} = \frac{h^3}{3\,\rho\,\nu}\left[\nabla\left(\gamma\nabla^2 h\right) + \rho\mathbf{g}\right], \tag{1}$$

where, in addition to the already introduced variables, $\mathbf{g} = g\mathbf{e}_x$ represents gravity, $\mathbf{q}$ is the fluid flux, and Φ_{evap} is the evaporative flux. The fluid flux $\mathbf{q}$ can be separated into two contributions, due to capillarity and gravity. Since the film is curved, there is a capillary pressure inside the liquid $\gamma\nabla^2 h$, the gradient of which is responsible for a capillary flow. Since the film is deposited on a vertical surface, the volumetric gravity force $\rho\mathbf{g}$ induces a gravity-driven flow.

When applying this equation to the films that are of interest in our study, we are able to make some simplifications. First, in our system, the film height always varies more intensely in the transverse than in the streamwise direction—typical measurement values of the slope in the transverse direction being of order 3×10^{-3}, to be compared with 5×10^{-5} in the vertical (streamwise) direction. This allows us to neglect spatial derivatives along the vertical direction ∂_x when compared to partial derivatives of similar order along the transverse direction ∂_z. Moreover, since we observe that the atmosphere in the channel is only slowly renewed, we can safely consider that the air inside the cell is saturated in liquid in vapor phase. This is confirmed by the fact that some extremely thin films (shallower than 0.5 μm)

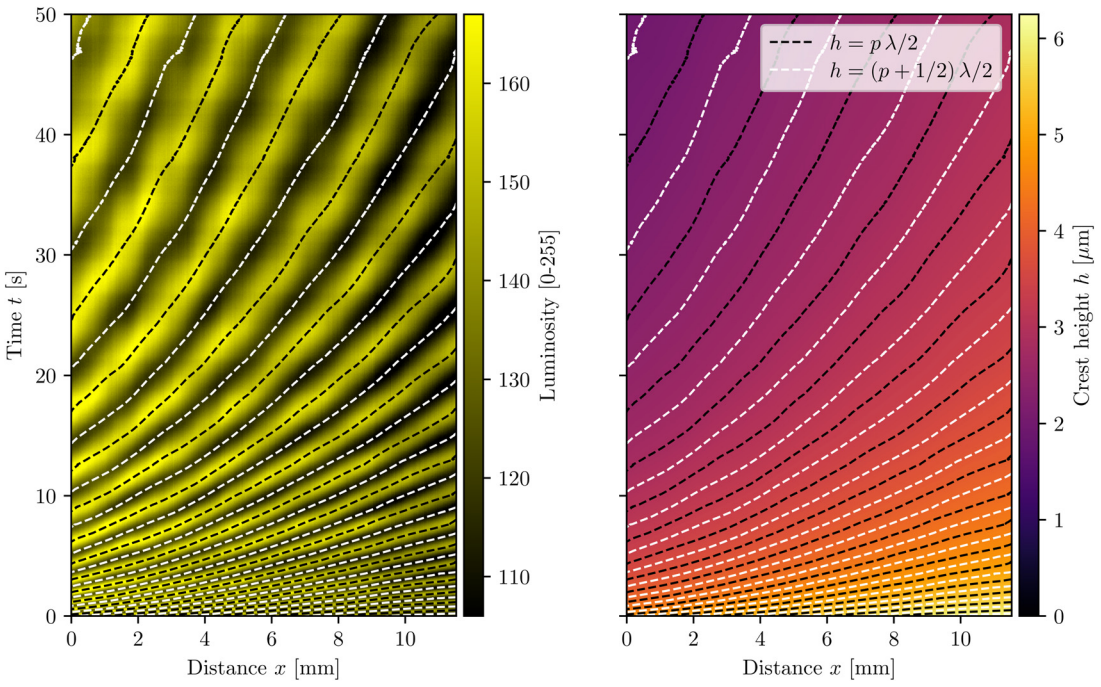

FIG. 4. Spatiotemporal evolution of the crest height. Left: Reference signal, i.e., normalized light intensity along the crest. Right: Height profile reconstructed by unwrapping the phase of the left signal. The black dashed line correspond to the $h = p\,\lambda/2$ isolines for all integers p (which should correspond to $\Phi = 2p\pi$, i.e., constructive interferences), and the white dashed lines to the $h = (p+1/2)\,\lambda/2$ isolines (for which $\Phi = \pi + 2p\pi$, i.e., destructive interferences). The lines are the same in the two plots, they are computed from the reconstructed height profile.

present in the field of view do not disappear during the experiment, although they drain no fluid and only evaporate. Thus, since we do not heat our system, the evaporation Φ_{evap} can be considered negligible in our case. Since we are interested in the evolution of the crest height $h_{crest}(x,t)$, for which $\partial_z h = 0$ (by definition), we obtain

$$\frac{\partial h}{\partial t} = -\frac{g}{\nu}\frac{\ell_c^2 h^3}{3}\frac{\partial^4 h}{\partial z^4} - \frac{g}{\nu} h^2 \frac{\partial h}{\partial x} \quad \text{at } h = h_{crest}, \tag{2}$$

where ℓ_c is the capillary length $\sqrt{\gamma/(\rho g)}$. The change of height of the film at the crest is the sum of two contributions, which are related to flows of the different physical origins we discussed earlier: capillarity and gravity. The second term corresponds to advection of the crest profile, characterized by its slope $\partial_x h$, due to the gravity-driven Poiseuille flow. The first term represents the drainage of fluid toward the edges (or the center) of the film when there is an excess (or a lack) of curvature at the crest. It depends on the *snap* $\partial_{zzzz} h|_{h_{crest}}$ at the crest, which is the geometrical quantity that describes the rate of evolution of the radius of curvature. This snap term can be written $\partial_{zzzz} h = \epsilon/(R L^2)$, where R is the radius of curvature, L is the characteristic length over which the curvature evolves, and ϵ is equal to -1 if there is an excess of mass at the center of the film (the transverse profile is sharper than a parabola) and $+1$ if the mass is predominantly on the sides of the film, i.e., the film is "flatter" than a parabola.

Whether any of these terms dominate can be determined by using a dimensionless number comparing capillarity and gravity, which can be assimilated to the equivalent of a Bond number,

$$\mathrm{Bo} = \frac{3\,|\partial_x h|}{\ell_c^2\, h\, |\partial_{zzzz} h|} = |\partial_x h|\,\frac{3R}{h}\left(\frac{L}{\ell_c}\right)^2. \tag{3}$$

However, it is difficult to evaluate the order of magnitude of this number. Indeed, on the one hand, the film is very thin ($h \ll R$), because of the relatively low speeds at which the meniscus is driven. On the other hand, the film is very flat in the vertical direction ($|\partial_x h| \ll 1$), because the amplitude of rivulet movement varies weakly along the x direction. Hence, we can not easily conclude *a priori*, and we must experimentally measure the geometric properties of the film to determine which of the two effects dominates the film drainage.

The measurement of $\partial_x h_{crest}$ is straightforward as it corresponds to the measurement of the spacing between interference fringes along the crest. The measurement of the *snap* $\partial_{zzzz} h$, however, is much more subtle because it requires the estimation of the fourth derivative of an experimental signal. It is always a challenge to estimate quantitatively and with acceptable accuracy such a high-order derivative of a noisy signal. Thanks to the high accuracy of the interferometric method, we are able to extract a meaningful measurement of this quantity and its uncertainty, as displayed in Supplementary Fig. Sf1. The resulting measurements of the mean value of h, $\partial_x h$, and $\partial_{zzzz} h$ can be seen in Supplementary Fig. SF.[2] From these measurements, we are able to compute the magnitude of both terms on the right-hand side of Eq. (2). Since our time resolution allows it, we can also compute $\partial_t h$ with a comparable accuracy, in order to verify our predictions. The comparison between the direct measurement of the height decrease and the computed effects due to capillarity and gravity can be seen in Fig. 5.

As can be seen in Fig. 5, in the case of a snapping motion, the dominant effect in crest height decrease is capillarity. Indeed, the excess curvature at the center of the film pushes the fluid outward toward the edges. This adds to the gravitational drainage due to the fact that the film is on a vertical plate. The opposite of this situation, where a lack of curvature at the center drives the liquid inwards, can be seen, for example, when studying the draining of a fluid on a narrow vertical plate.[35]

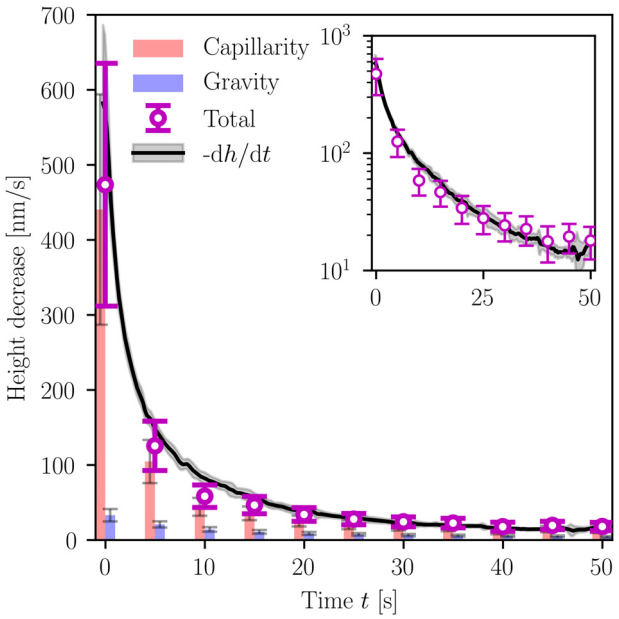

FIG. 5. Drainage of the crest of the film as a function of time, with contribution from both capillarity (red, bars on the left) and gravity (blue, bars on the right). The purple points "Total" are the sum of capillary and gravity-driven drainage. The black line corresponds to the direct measurement of $\partial h/\partial t$. Inset: semi-log scale showing the agreement is excellent even for small drainage.

Our technique thus allows us to quantitatively measure geometrical characteristics of thin films, with excellent accuracy in both space and time. This is showcased by our ability to accurately measure the time evolution of the films down to tens of nanometers per second and link it to their physical causes.

V. CONTROLLED DEPOSITION

Another interest of our setup is the ability to decide the initial characteristics of the deposited film by controlling the movement imposed on the rivulet. Indeed, since the films are deposited by the menisci on the edges of the rivulet, pushing it at a controlled speed leads to the deposition of a film of deterministic thickness. To illustrate this approach, in this section, we drive the rivulet back and forth periodically in the transverse direction using speakers on the side of the cell. By measuring independently the deposition speed and film thickness, we confirm that we can predict the depth of the resulting film.

Since the incident light is strongly refracted by the menisci on the side of the rivulet, luminosity is minimal—only light reflected on the first glass pane surfaces (air–glass and glass–oil) reaches the lens—so the menisci appear as dark bands [Fig. 6(a)]. The luminosity is slightly higher in the center region that additionally receives light from the out-of-focus back glass pane, but it is still darker than outside the rivulet where additional reflections on high optical contrast oil–air interfaces contribute. For a given x position, by looking at the luminosity

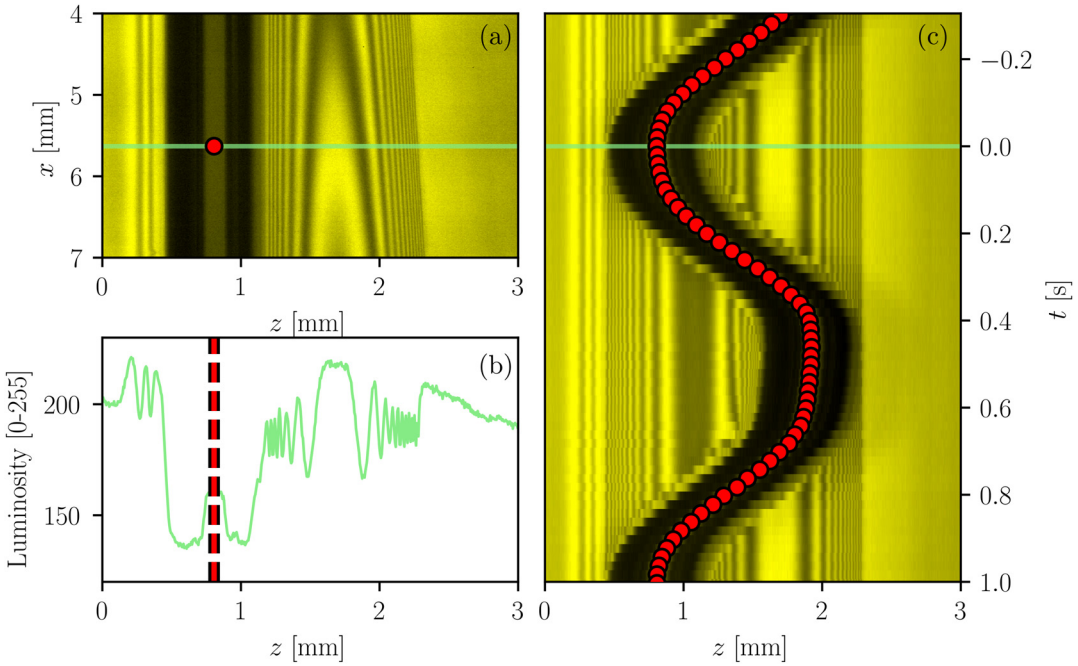

FIG. 6. Extraction of the position of the rivulet on the image. (a) Experimental image for $t = 0$. Green is the position x_3 that we consider. The black and red dot is the (detected) position of the rivulet. (b) Luminosity profile for $x = x_3$ with the rivulet position in black and red dashed line. (c) Slice of the image for $x = x_3$ as a function of time, with the position of the rivulet.

profile [Fig. 6(b)], we can then find the center of the rivulet z_c. This is done using an algorithm by fitting a heuristic idealized profile to the experimental luminosity data. By using this approach for different frames, we are able to monitor how z_c evolves with time [Fig. 6(c)]. This allows us to measure experimentally the amplitude of the movement as well as the instantaneous speed of the rivulet. Since the rivulet is to a good approximation of constant width, this speed corresponds to the deposition speed of the menisci, which dictates the deposited film height.

When looking at the luminosity profile for a given x coordinate we can also identify the zone over which the film extends. This corresponds to the grayed-out zone in Fig. 7(a). Note that near the rivulet meniscus, light intensity drops and interference fringes are not resolved, due to the large interface slope. Measuring the height profile in this region requires a camera/lens system with a larger numerical aperture and a larger spatial resolution.

We then use an algorithm to find the maxima and minima of luminosity, i.e., the position of the bright and dark fringes resulting from constructive and destructive interference. To obtain the phase, we can associate each of the extrema to a phase shift of π and plot the result as a function of the transverse coordinate as shown in Fig. 7(b).

Lastly, note that it is possible to obtain information on the height in regions where the fringes are between dark and bright, i.e., to achieve sub-fringe resolution. To this end, an analytic signal is constructed by means of the Hilbert transform on the luminosity signal. From the local phase of this signal, the interpolated profile is then computed and represented as a continuous line in Fig. 7(b). This allows for a spatially well-resolved measurement of the film height h. Note the scale of the bottom axis for Fig. 7(b): we use the distance relative to the rivulet center, which allows us to make meaningful comparisons between profiles at different x positions.

For the experiments in this section, we use static elements in the cell that are designed to focus the flow of air generated by the speakers in a particular region (see Supplementary Fig. Sf4). This creates an inhomogeneous forcing, where the displacement of the rivulet depends on the x coordinate. Since the amplitude of the movement of the rivulet depends on space, so does the speed at which it moves and thus the height of the film it deposits. An illustration of this is presented in Fig. 8. On the left, we see the image of reference ($t = 0$) from which we extract the height profile $h(z)$ for different x positions $x_{1,2,\ldots}$. As for Fig. 7, the empty circles correspond to dark or bright fringes, and the full lines to the unwrapped instantaneous phases of the analytic signals obtained by Hilbert transforms. One might remark that in Fig. 8(b), the top of the profiles is one fourth of a wavelength from each other. This is due to the fact that the selected positions $x_{1,2,\ldots}$ are on dark and bright interference fringes, alternatively.

Figure 8(c) is a parametric plot of the z-wise velocity of the rivulet center $\mathrm{v}(t)$ as a function of its position $z(t)$ over time $-T/2 < t < 0$, with T being the period of the movement. One can see by comparing Figs. 8(b) and 8(c) that at the x positions where the rivulet went faster, it deposited a higher film. Note that since the velocity is measured for the center of the rivulet, the two bottom axes do not correspond to one another: the height and speed curves are shifted with respect to one another. The shift corresponds to the distance between the center of the rivulet and the point where the film detaches from the meniscus. We measure this shift to be $340 \pm 10\,\mu\mathrm{m}$, which is coherent with the fact that menisci are arcs of circles of radius 300 μm, and that the distance between the two menisci is around 100 μm.

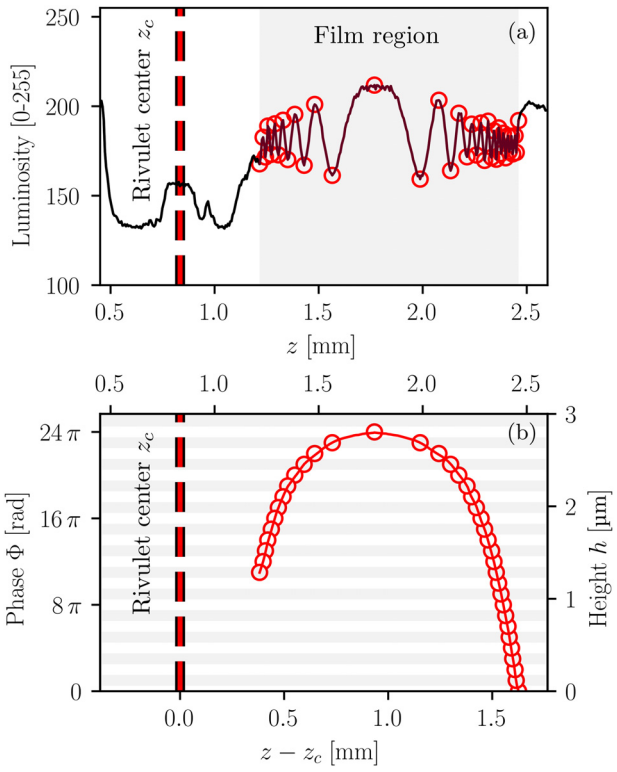

FIG. 7. (a) Luminosity profile as a function of the transverse coordinate z at $x = x_3$. In gray, the zone of interest over which the thin film extends. The empty circles correspond to extrema. (b) Phase/height profile as a function of absolute/relative transverse coordinate.

We now want to quantitatively make a link between the rivulet speed and the deposited film height. This situation is analogous to the Landau–Levich–Derjaguin problem of film deposition by a static meniscus onto a moving plate, in a confined geometry where the curvature of the meniscus is not determined by gravity but by the geometry of our cell. To characterize the speed of the moving interface, we thus follow LLD and use the capillary number $\mathrm{Ca} = \rho\,\nu\,|\dot{z}_c|/\gamma$; and the height of the deposited film is normalized by the curvature radius of the static meniscus $b/2$ so that we are interested in $h^* = h/(b/2)$.

The height of the liquid film deposited should then be given by $h^* = 1.34\,\mathrm{Ca}^{2/3}$, which is the classical LLD scaling.[17,18,36] We plot in Fig. 9 the dimensionless height as a function of the capillary number, as well as the LLD scaling with the theoretically predicted prefactor. We find perfect agreement between our experimental measurements and the LLD prediction, confirming our ability to generate films of deterministic height by controlling the rivulet speed.

One last point to take into consideration is the stability of these films. In Sec. IV, we studied a film generated by using a snapping motion of the rivulet. This implied a very fast reconfiguration of the film geometry, with the film height diminishing as fast as 100 nm/s. For the data presented in this section, the rivulet adopts a smooth movement with an amplitude that varies very slowly with the x coordinate. As a consequence, the draining is expected to be, and indeed is, much slower.

To measure the film thinning by drainage, it can be advantageous to correlate the luminosity signal along the crest line for different times, rather than directly evaluating the time derivative of the $h_{\mathrm{crest}}(x,t)$ field as done in Sec. IV. The correlation is performed on images where the moving meniscus is far from the crest line so that the latter evolves only through drainage. This technique remains accurate even at very low fringe displacement speed, of order 100 μm/s, which corresponds to less than half a pixel per frame. In our test case, we estimate the height decrease at the crest to be 9 ± 1 nm/s—the measurement being done over a time of only 0.2 s. Being able to accurately measure such small quantities with an excellent temporal resolution using a macroscopic observation method is a testimony to the precision of our measurement technique.

VI. CONCLUSION/PERSPECTIVES

In this article, we have exposed a powerful way to deterministically create and study with precision very thin films of liquid over a rigid plate. By injecting oil into an air-filled Hele–Shaw channel, we generate a rivulet of liquid presenting two menisci of fixed curvature. By pushing air into the cell, we are able to impose a transverse movement on the rivulet and thus the displacement speed of the menisci. This leads to the deposition of a film whose height is controlled by the velocity of the menisci and their curvature (determined by the chosen cell spacing).

In the range of capillary numbers explored here ($10^{-5} < \mathrm{Ca} < 10^{-3}$) the film thickness is accurately predicted by the classical Landau–Levich–Derjaguin theory. This is not trivial as the velocity is varied in one sweep over a short time interval of $T/4 = 250$ ms. To the best of our knowledge, there are so far no experimental studies that have explored the entrainment problem with an accelerating meniscus. By providing maximum velocity and acceleration timescale as separate control parameters, our setup is ideally suited to disentangle two effects that cause departure from the LLD scaling at large velocities, namely inertial and boundary layer effects.[16]

On the one hand, inertia leads to a divergence of the deposited film in the case of substrates extracted from a bath. Indeed, when the dynamic pressure $\rho|\mathbf{v}|^2$ exceeds the capillary pressure drop in the dynamic meniscus region, of order $\sim \gamma/b$, the latter cannot prevent the liquid bulk from entering the film region. This transition is thus controlled by the Weber number $\mathrm{We} = \rho|\mathbf{v}|^2 b/\gamma$, that can be readily varied over orders of magnitude through the velocity $|\mathbf{v}|$.

On the other hand, the viscous boundary layer of entrained fluid thins with increasing velocity in the case of substrates extracted from a bath, or with stronger acceleration in our setup. This should *decrease* the height of the deposited film, as $\sqrt{\nu T/4}$ in our case.

Both divergence and thinning are observed consecutively in the case of substrates extracted from a bath,[16] where the main control parameter (velocity) affects both transitions. In our system, the Weber number and the boundary layer thickness are separately controllable, which should allow future studies exploring regimes where either effect is important and the other not. For the data in this paper, $\mathrm{We} \simeq 1 \times 10^{-3} \ll 1$ and $\sqrt{\nu T/4} \simeq 1\,\mathrm{mm} \simeq b$, so neither dynamical pressure nor boundary layer thinning comes into play.

Using an interferometric method, we can measure the film height in the whole region visible to the camera where the film is weakly inclined. This measurement is instantaneous, so the spatiotemporal evolution of these films can be monitored with a resolution limited only by the camera capabilities. Thanks to these accurate

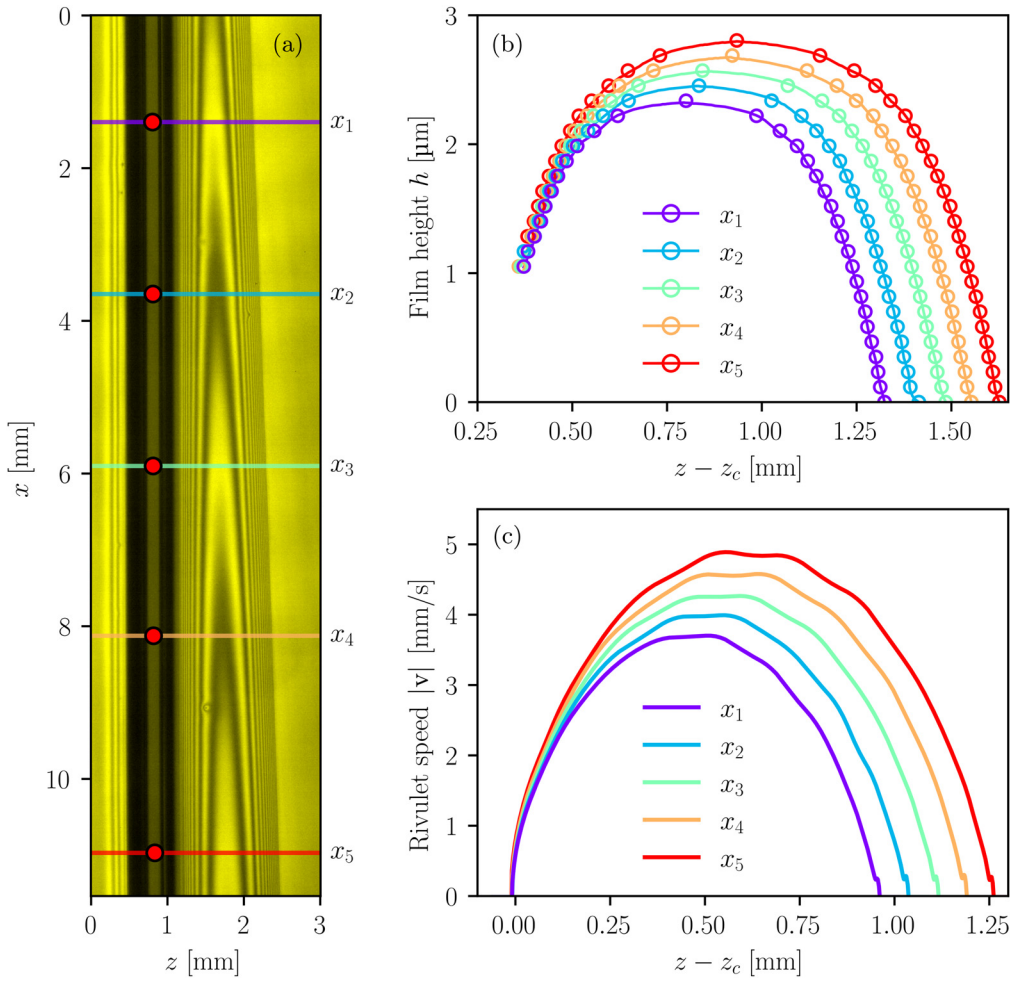

FIG. 8. (a) The reference image, with the positions of interest (colored strips). The rivulet position z_c is indicated by red circles. (b) The height of the film at the positions of interest as a function of the transverse coordinate relative to the rivulet position. (c) Speed of the rivulet as a function of relative position [same scale as (b)].

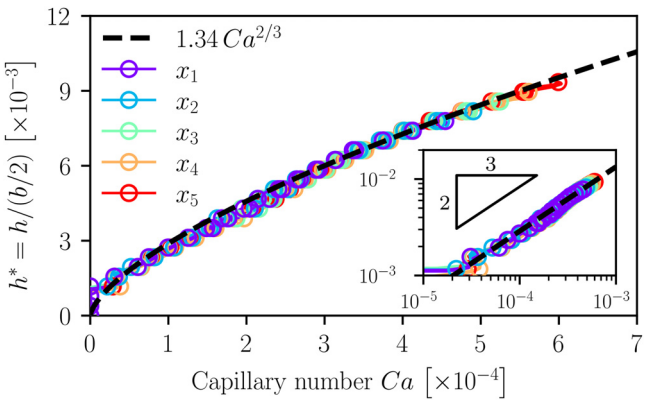

FIG. 9. Height of the film deposited by a periodic motion of the rivulet as a function of the capillary number. The dashed line corresponds to the LLD prediction. Inset: Same data on logarithmic scale.

measurements, we are able, for example, to predict the height decrease in a film and to attribute it to the combination of capillary and gravitational effects.

There are, of course, limitations on the accuracy of our methods. When using a rivulet confined in a Hele–Shaw cell, one must stay below a certain flow rate to avoid spontaneous meandering.[32] One must also ensure not to move the rivulet too fast with too much amplitude, lest the rivulet be prone to a phase-locking instability.[33] Fast image acquisition necessitates a powerful monochromatic light source.

The interferometric method imposes a trade-off between precision on height measurement and the ability to explore high-slope regions of the film. Indeed, when using small wavelength light, the better height resolution comes at the cost of having very thin fringes in the most inclined parts of the film. Optically resolving such thin fringes requires excellent spatial resolution, which is not always available. On the contrary, using long-wavelength light allows one to see a greater region of the film, at the cost of reduced precision on the height measurement over the flatter parts.

There are also ways to improve the technique we present here, or adapt it to study other situations. Concerning film generation, the use of a fluid rivulet confined in a cell imposes the Hele–Shaw geometry with two plates. It would, however, be possible to adapt this work using a fluid rivulet flowing on a single plate or using sliding droplets. To move the rivulet, we use speakers, which have a limited stroke. Replacing the speakers with compressed air nozzles controlled by valves would allow for a greater movement amplitude and a finer spatial control of the rivulet motion. Using a heated plate and renewing the air inside the cell would also allow for evaporation to occur, which can be useful to cure the deposited film or enhance heat exchange in industrial applications.[37]

SUPPLEMENTARY MATERIAL

See supplementary material for four figures, labeled SF1–SF4. They provide information on the *snap* measurement (SF1 and SF2), the film drainage (SF2 and SF3), the luminosity images correlation (SF3), and an illustration of the immobile obstructing elements in the cell (SF4).

ACKNOWLEDGMENTS

The research received special funds from the Laboratory MSC UMR 7057.

AUTHOR DECLARATIONS

Conflict of Interest

The authors have no conflicts to disclose.

Author Contributions

G. Le Lay: Conceptualization (lead); Data curation (lead); Formal analysis (lead); Investigation (lead); Methodology (equal); Software (equal); Visualization (lead); Writing – original draft (lead); Writing – review & editing (equal). **A. Daerr:** Funding acquisition (lead); Methodology (equal); Project administration (lead); Software (equal); Supervision (lead); Validation (lead); Writing – original draft (supporting); Writing – review & editing (equal).

DATA AVAILABILITY

All the source code and analysis routines used to obtain the figures in this article, as well as the relevant raw data, are available in an open-access repository.[34]

REFERENCES

[1]R. D. Deegan, O. Bakajin, T. F. Dupont, G. Huber, S. R. Nagel, and T. A. Witten, "Capillary flow as the cause of ring stains from dried liquid drops," Nature **389**, 827–829 (1997).
[2]G. Berteloot, A. Hoang, A. Daerr, H. Kavehpour, F. Lequeux, and L. Limat, "Evaporation of a sessile droplet: Inside the coffee stain," J. Colloid Interface Sci. **370**, 155–161 (2012).
[3]P. Angeli and A. Gavriilidis, "Hydrodynamics of Taylor flow in small channels: A review," Proc. Inst. Mech. Eng., Part C: J. Mech. Eng. Sci. **222**, 737–751 (2008).
[4]J. B. Grotberg, "Respiratory fluid mechanics," Phys. Fluids **23**, 021301 (2011).
[5]M. Baudoin, Y. Song, P. Manneville, and C. N. Baroud, "Airway reopening through catastrophic events in a hierarchical network," Proc. Nat. Acad. Sci. U. S. A. **110**, 859–864 (2013).
[6]X. Zhang and V. S. Nikolayev, "Liquid film dynamics with immobile contact line during meniscus oscillation," J. Fluid Mech. **923**, A4 (2021).
[7]J. Zhang, Z. Hou, and C. Sun, "Theoretical analysis of the pressure oscillation phenomena in capillary pumped loop," J. Therm. Sci. **7**, 89–96 (1998).
[8]V. S. Nikolayev, "Physical principles and state-of-the-art of modeling of the pulsating heat pipe: A review," Appl. Therm. Eng. **195**, 117111 (2021).
[9]S. Launay, V. Platel, S. Dutour, and J.-L. Joly, "Transient modeling of loop heat pipes for the oscillating behavior study," J. Thermophys. Heat Transfer **21**, 487–495 (2007).
[10]F. Goucher and H. Ward, "A problem in viscosity," Phil. Mag. **44**, 1002–1014 (1922).
[11]F. C. Morey, "Thickness of a liquid film adhering to a surface slowly withdrawn from the liquid," J. Res. Nat. Bur. Stand. **25**, 385 (1940).
[12]D. Lasseux and M. Quintard, "Epaisseur d'un film dynamique derrière un ménisque récessif," Méc Fluids **II**(313), 1375–1381 (1991).
[13]D. Quéré, A. de Ryck, and O. O. Ramdane, "Liquid coating from a surfactant solution," Europhys. Lett. **37**, 305 (1997).
[14]R. M. Davies and G. I. Taylor, "The mechanics of large bubbles rising through extended liquids and through liquids in tubes," Proc. R. Soc. London. Ser. A, Math. Phys. Sci. **200**, 375–390 (1950).
[15]F. P. Bretherton, "The motion of long bubbles in tubes," J. Fluid Mech. **10**, 166–188 (1961).
[16]D. Quéré, "Fluid coating on a fiber," Annu. Rev. Fluid Mech. **31**, 347–384 (1999).
[17]L. Landau and B. Levich, "Dragging of a liquid by a moving plate," in *Dynamics of Curved Fronts*, edited by P. Pelcé (Academic Press, San Diego, 1942), pp. 141–153.
[18]B. Derjaguin, "On the thickness of the liquid film adhering to the walls of a vessel after emptying," Prog. Surf. Sci. **43**, 134–137 (1993).
[19]D. A. White and J. A. Tallmadge, "Theory of drag out of liquids on flat plates," Chem. Eng. Sci. **20**, 33–37 (1965).
[20]K. J. Ruschak, "Coating flows," Annu. Rev. Fluid Mech. **17**, 65–89 (1985).
[21]A. Q. Shen, B. Gleason, G. H. McKinley, and H. A. Stone, "Fiber coating with surfactant solutions," Phys. Fluids **14**, 4055–4068 (2002).
[22]G. F. Teletzke, H. T. Davis, and L. E. Scriven, "Wetting hydrodynamics," Rev. Phys. Appl. (Paris) **23**, 989–1007 (1988).
[23]J. H. Snoeijer, "Avoided critical behavior in dynamically forced wetting," Phys. Rev. Lett. **96**, 174504 (2006).
[24]A. De Ryck and D. Quéré, "Inertial coating of a fibre," J. Fluid Mech. **311**, 219–237 (1996).
[25]S. Lips, A. Bensalem, Y. Bertin, V. Ayel, C. Romestant, and J. Bonjour, "Experimental evidences of distinct heat transfer regimes in pulsating heat pipes (PHP)," Appl. Therm. Eng. **30**, 900–907 (2010).
[26]J. H. Snoeijer, "Thick films of viscous fluid coating a plate withdrawn from a liquid reservoir," Phys. Rev. Lett. **100**, 244502 (2008).
[27]L. Fourgeaud, V. S. Nikolayev, E. Ercolani, J. Duplat, and P. Gully, "In situ investigation of liquid films in pulsating heat pipe," Appl. Therm. Eng. **126**, 1023–1028 (2017).
[28]Y. J. Youn, Y. Han, and N. Shikazono, "Liquid film thicknesses of oscillating slug flows in a capillary tube," Int. J. Heat Mass Transfer **124**, 543–551 (2018).
[29]L. Zheng, Y.-X. Wang, J. L. Plawsky, and P. C. Wayner, "Accuracy of measurements of curvature and apparent contact angle in a constrained vapor bubble heat exchanger," Int. J. Heat Mass Transfer **45**, 2021–2030 (2002).
[30]P. G. Saffman and G. I. Taylor, "The penetration of a fluid into a porous medium or Hele-Shaw cell containing a more viscous liquid," Proc. R. Soc. London A, Math. Phys. Sci. **245**, 312–329 (1958).
[31]P. Tabeling, G. Zocchi, and A. Libchaber, "An experimental study of the Saffman-Taylor instability," J. Fluid Mech. **177**, 67–82 (1987).
[32]A. Daerr, J. Eggers, L. Limat, and N. Valade, "General mechanism for the meandering instability of rivulets of Newtonian fluids," Phys. Rev. Lett. **106**, 184501 (2011).
[33]G. L. Lay and A. Daerr, "Phase-locking parametric instability coupling longitudinal and transverse waves on rivulets in a Hele-Shaw cell," Phys. Rev. Lett. **134**, 014001 (2025).
[34]G. Le Lay and A. Daerr, *Data Analysis for Thin Films Measurements* (Zenodo, 2025).
[35]N. Xue and H. A. Stone, "Gravitational drainage on a vertical substrate of a narrow width," Phys. Rev. Fluids **7**, 014001 (2022).
[36]I. Cantat, "Liquid meniscus friction on a wet plate: Bubbles, lamellae, and foams," Phys. Fluids **25**, 031303 (2013).
[37]L. Pagliarini, N. Iwata, and F. Bozzoli, "Pulsating heat pipes: Critical review on different experimental techniques," Exp. Therm. Fluid Sci. **148**, 110980 (2023).